Check for updates

Energy Technology
Generation, Conversion, Storage, Distribution
www.entechnol.de

The Elemental Multifariousness of the Defect-Pyrochlore Crystal Structure and Application in Photocatalytic Hydrogen Generation

*Morten Weiss, Gerald Hoerner, Birgit Weber, and Roland Marschall**

Tungsten-based defect-pyrochlores $CsM_xW_{2-x}O_6$ are used as model oxides to investigate the high number of possible M cations that can be used to form the defect-pyrochlore crystal structure. A large variety of possible compounds are presented, several of which have been unknown so far. These compounds are used in photocatalytic hydrogen evolution to investigate possible correlations between the photocatalytic activity and the varying elemental compositions.

1. Introduction

Defect-pyrochlores (sometimes also called β-pyrochlores) were first published by Babel et al. in 1967[1] and have been used ever since in a wide range of applications, such as ion conduction,[2–5] electronic conductivity,[6–8] thermoelectricity,[9,10] superconductivity,[11] luminescence,[12–14] ion exchange for environmental remediation,[15] and photocatalysis.[16–21]

Defect-pyrochlores have the general formula $AM_xM'_{2-x}X_6$, in which A is an alkali metal cation (K^+, Rb^+, Cs^+) or Tl^+, M and M′ are transition or main-group metal cations, and X is O^{2-} and/or F^-.[1,22] Defect-pyrochlores are different in their crystal structure from normal pyrochlores (or α-pyrochlores) $A_2M_2X_6X'$, in which A can also be an alkali-earth or rare-earth cation.[23] Removal of half of the A cations and the X′ anion (O^{2-} or F^-) results in the loss of the A_2X network—which is interpenetrated by the M_2X_6 network—and the formation of the defect-pyrochlore structure: the crystal structure of defect-pyrochlores is also cubic (space group $Fd\bar{3}m$, number 227) with M and M′ statistically distributed on identical 16*c* (0, 0, 0) sites and O on 48*f* (*x*, 1/8, 1/8) sites.[24] M and M′ are octahedrally coordinated by O, with the corner-sharing octahedra forming hexagonal channels (**Figure 1**a). The A cations are located within these channels, and the exact position depends on the size of the cation: K^+ is located on one quarter of 32*e* (*x*, *x*, *x*) sites, whereas Rb^+ and Cs^+ are located on 8*b* (3/8, 3/8, 3/8) sites.[23–26] Incorporation of water molecules has also been observed for some K^+-containing defect-pyrochlores, but not for Rb^+- or Cs^+-containing ones; water incorporation in $RbNbWO_6$ has only been observed at elevated pressures.[23,25,27–29]

Because M and M′ occupy the same site, it is possible to use M cations with varying oxidation states to form the defect-pyrochlore crystal structure if charge balance is maintained by adjusting the M/M′ ratio (Figure 1b). The resulting general formulas are $AM_1M'_1O_6$ for M^{5+},[1,26,30–36] $AM_{0.5}M'_{1.5}O_6$ for M^{4+},[6,22,37,38] $AM_{0.33}M'_{1.67}O_6$ for M^{3+},[6–8,10,13,39–41] $AM_{0.25}M'_{1.75}O_6$ for M^{2+},[6,37] and $AM_{0.2}M'_{1.8}O_6$ for M^{1+}.[37] In these examples, M′ is a hexavalent cation, such as Mo^{6+}, Te^{6+}, or W^{6+}. We have chosen to use W^{6+}-based defect-pyrochlores in this work because Mo^{6+}-containing defect-pyrochlores are unsuitable for hydrogen evolution due to the low conduction band (CB) position.[18] Moreover, Te^{6+}-containing defect-pyrochlores are susceptible to photocorrosion, which we have shown in our previous work.[42] Cs^+ has been used as an A cation instead of K^+ to avoid possible water incorporation.

In this work we synthesize $CsM_xW_{2-x}O_6$ compounds via an aqueous sol–gel reaction followed by solution combustion, which was first published by Schwertmann et al.[17] The advantages of this synthesis, as compared to conventional solid-state reaction, are the mixing of the metal precursors on an atomic scale—thus precluding diffusion problems—and the lower reaction temperatures and times. We used these advantages to synthesize a comprehensive library of $CsM_xW_{2-x}O_6$ defect-pyrochlores to investigate the elemental diversity of the defect-pyrochlore crystal structure. Then, this library was used to find potential correlations between elemental composition and photocatalytic activity of $CsM_xW_{2-x}O_6$ in sacrificial hydrogen evolution. Of special interest is the use of first-row transition elements with partially occupied *d*-levels as M cations—that is, Cr^{3+}, Mn^{2+}, Fe^{3+}, Ni^{2+}; Co^{2+}, and Cu^{2+}, because defect-pyrochlores containing Cr^{3+} and Fe^{3+} have been reported to have reduced bandgaps compared to defect-pyrochlores with unoccupied *d*-levels, such as $CsNbWO_6$ or $CsTaWO_6$, and are reported to be photocatalytically active in visible light.[43,44] Using the aforementioned synthesis, it is possible to synthesize materials with tailored bandgaps in the visible light region using different M cations.

M. Weiss, G. Hoerner, B. Weber, R. Marschall
Department of Chemistry
University of Bayreuth
95440 Bayreuth, Germany
E-mail: roland.marschall@uni-bayreuth.de

The ORCID identification number(s) for the author(s) of this article can be found under https://doi.org/10.1002/ente.202100302.

© 2021 The Authors. Energy Technology published by Wiley-VCH GmbH. This is an open access article under the terms of the Creative Commons Attribution License, which permits use, distribution and reproduction in any medium, provided the original work is properly cited.

DOI: 10.1002/ente.202100302

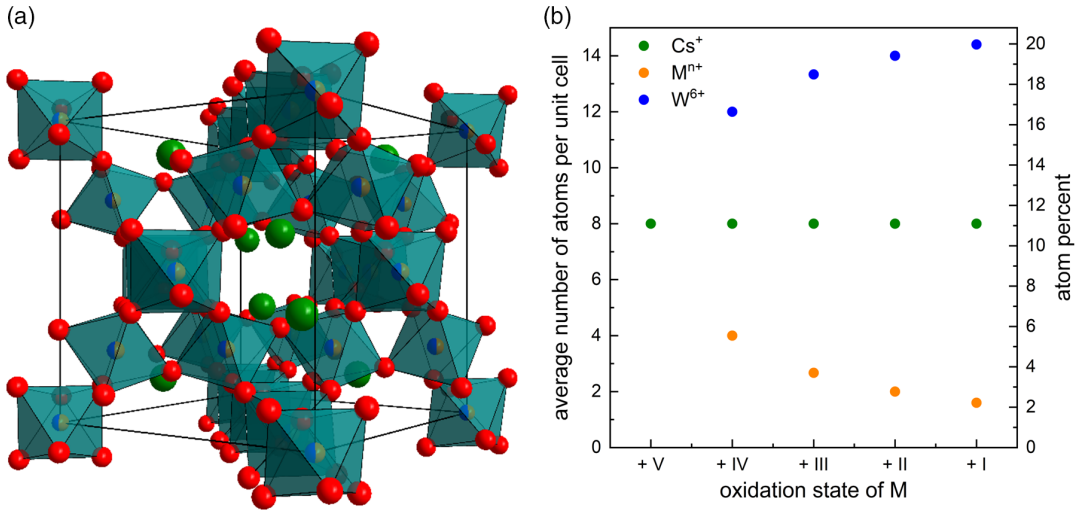

Figure 1. a) Crystal structure of $CsM_xW_{2-x}O_6$ (green: Cs^+, orange: M^{n+}, blue: W^{6+}, red: O^{2-}). b) Number of metal atoms per unit cell; the number of oxygen atoms per unit cell is constantly 48.

2. Results and Discussion

2.1. Structural Characterization

Seventeen different phase-pure $CsM_xW_{2-x}O_6$ compounds could be obtained via sol–gel synthesis followed by combustion and annealing at high temperatures. To the best of our knowledge, the compounds $CsLi_{0.2}W_{1.8}O_6$, $CsM_{0.25}W_{1.75}O_6$ ($M = Mg^{2+}$, Mn^{2+}, Co^{2+}, Ni^{2+}, Cu^{2+}, and Zn^{2+}) and $CsIn_{0.33}W_{1.67}O_6$ are reported here for the first time. High crystallinity prevails for all samples as is exemplarily shown with one sample for every oxidation state of M (**Figure 2**). Characterization for the other samples can be found in the Supporting Information (Figure S1, Supporting Information); all reflections visible in the X-ray diffraction (XRD) pattern can be ascribed to those calculated for defect-pyrochlores. The reflection positions are slightly different for each sample, indicating a change of the lattice constant; this is discussed in detail further subsequently. Also, broadening of the reflections for some samples is observed, indicating changing crystallite sizes. The crystallite sizes are rather different for all samples (Figure S2, Supporting Information); however, the smallest crystallite sizes have been observed for the cations with the greatest charge, i.e., Nb^{5+} and Ta^{5+}.

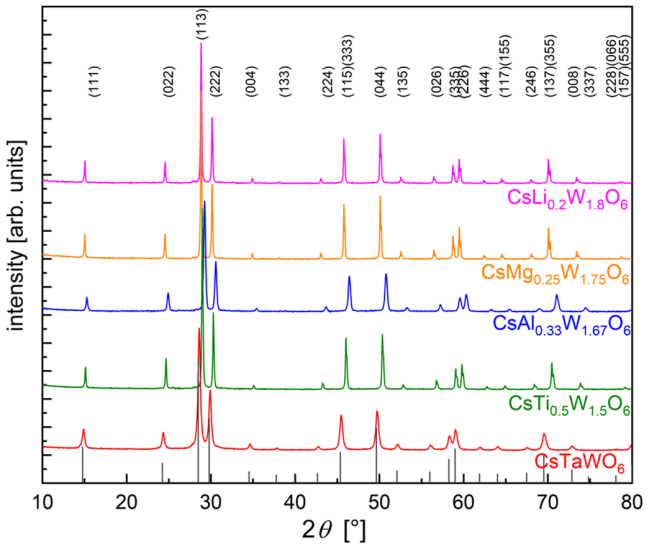

Figure 2. XRD patterns of selected samples after annealing at 800 or 900 °C for $CsLi_{0.2}W_{1.8}O_6$.

All samples have been annealed in a temperature range from 500 to 900 °C to investigate their formation temperature and thermal stability; the respective diffraction patterns can be seen in Figure S3–S5, Supporting Information. Most samples are already crystalline after combustion (labelled as-syn.); however, these samples are colored black due to carbon residues from EDTA and citric acid (not shown). Annealing in air is necessary to completely remove the carbon and to ensure a high crystallinity of all samples. Although most samples are already phase-pure after annealing at 500 °C, some samples, such as $CsCu_{0.25}W_{1.75}O_6$ and $CsNi_{0.25}W_{1.75}O_6$, require slightly higher temperatures (Figure S3, Supporting Information). One exception is $CsLi_{0.2}W_{1.8}O_6$, which requires 850 °C to become phase-pure (Figure S3, Supporting Information); at lower temperatures reflections belonging to $CsLiWO_4$ can be observed. This is in contrast to $CsZr_{0.5}W_{1.5}O_6$ and $CsHf_{0.5}W_{1.5}O_6$, where additional reflections can be observed above 750 and 600 °C, respectively (Figure S5, Supporting Information). In addition, the compounds $CsM_{0.33}W_{1.67}O_6$ ($M = Sc^{3+}$ and Sb^{3+}), $CsM_{0.5}W_{1.5}O_6$ ($M = Ge^{4+}$ and Sn^{4+}), and $CsVWO_6$ (Figure S6, Supporting Information) were obtained; however, these could not be obtained phase-pure in the aforementioned temperature range. The synthesis of $CsVWO_6$ via solid-state reaction has been reported before;[1,35] however, our attempts to synthesize phase-pure $CsVWO_6$ this way have also been in vain (not shown). The existence of $CsSbWO_6$ (with $M = Sb^{5+}$) has also been reported[35] but has not been included in this work due to lack of a suitable Sb(V) precursor for our synthesis. CsW_2O_6, with

© 2021 The Authors. Energy Technology published by Wiley-VCH GmbH

both W^{5+} and W^{6+} cations, has also been reported[45–47] but access to a W^{5+}-containing mixed valence compound should be impossible with the synthesis described herein due to the inherent susceptibility of W^{5+} toward oxidation upon combustion and annealing in air. We have also attempted to synthesize the hypothetical compounds $CsM_{0.33}W_{1.67}O_6$ ($M = Y^{3+}$, La^{3+}, and Bi^{3+}), but no defect-pyrochlore was formed; instead mixtures of other phases were obtained (Figure S7, Supporting Information), the likely reason is that these cations are too large.

The shifts of the reflections observed in Figure 2 indicate a change of the lattice constant for different M cations. To elucidate this effect, Rietveld refinements were performed for the samples, including those with impurities (Figure S8–S11, Supporting Information). The generally good agreement between the observed and calculated intensities further supports the defect-pyrochlore type to be the common crystal structure of all these samples. A nearly linear correlation between the lattice constant and the ionic radius of M can be observed (**Figure 3**a): to compensate for the different M/W ratios, weighted average ionic radii of M/W were used instead of simply using the ionic radius of the M cations. A similar linear correlation has been observed by Castro et al. for the series $CsM_{0.5}W_{1.5}O_6$ ($M = Ti^{4+}$, Zr^{4+}, and Hf^{4+}).[22] The comparatively smaller lattice constant for $M = Sb^{3+}$ is likely a consequence of the lone pair of Sb^{3+}. To exclude a possible oxidation to Sb^{5+}, X-ray photoelectron spectroscopy (XPS) measurements were performed (Figure S12, Supporting Information): although the analysis is complicated due to the total overlap between O 1*s* and Sb $3d_{5/2}$, peak fitting is possible using the Sb $3d_{3/2}$ signal and constraints to accurately fit the Sb $3d_{5/2}$ peak. Binding energies for Sb 3*d* are 530.5 and 539.9 eV, respectively; comparing these values with the literature indicates the presence of Sb^{3+} and not of Sb^{5+}.[48] A detailed discussion of the O 1*s* signals of defect-pyrochlores can be found in our previous publication.[42]

Also noteworthy are the large lattice constants of $CsMWO_6$ ($M = Nb^{5+}$ and Ta^{5+}), especially compared to the reported lattice constant of $CsSbWO_6$ (with Sb^{5+}, ionic radius is 0.6 Å) of 10.2867 Å.[35] The even larger lattice constant of $KNbWO_6$ has been reported to be 10.5068 Å;[23] however, this results from the incorporation of water molecules into the hexagonal channels of the crystal structure, which has not been observed for $CsTaWO_6$.[29]

From the Rietveld refinements the interatomic distances of all phase-pure compounds have also been determined (Figure 3b). The average M/W—O distance of all compounds are very similar to each other: 1.96 Å < M/W—O distance < 2.02 Å, with only one outlier. They are also similar to those reported for other defect-pyrochlores such as $ANbWO_6$ ($A = H^+$, NH_4^+, K, and Rb), $KNbTeO_6$, and $KSbWO_6$.[23,25] The W—O distances observed in the defect-pyrochlores also fit rather well to the mean distance of 1.930 Å found for γ–WO_3 (in contrast to the defect-pyrochlores, the W—O distances within one octahedra are not uniform for γ–WO_3 and range from 1.732 to 2.186 Å).[49] The Cs—O distances are 0.4 Å larger than those reported for K^+-containing defect-pyrochlores,[23,25] which can be explained with the larger size of Cs^+ as compared to K^+. Compounds with a larger lattice constant ($M = Nb^{5+}$, In^{3+}, Hf^{4+}, and Ta^{5+}) also show an increased Cs—O distance.

For the ionic radii of Mn^{2+}, Fe^{3+}, and Co^{2+} data were plotted corresponding to the high-spin (HS) electronic configurations ($t_{2g}^3 e_g^2$ for Mn, Fe and $t_{2g}^5 e_g^2$ for Co, respectively), which are typical for octahedral coordination of weak-field donors such as oxido ligands. Validation of the selected spin state—and thus the ionic radius—stems from recording the effective magnetic moment μ_{eff} via magnetic measurements between 50 and 300 K (**Figure 4**a). Clearly, the magnetic moments of the samples are commensurable only with HS formulations. For instance, the samples with $M = Fe^{3+}$ or Co^{2+} show satisfying agreement with the spin-only values computed for three HS-d^5 or two HS-d^7 magnetically noninteracting ions, respectively (pink and green in Figure 4a). The μ_{eff} for Co(II) is, with regard to the spin-only value, larger than expected but reasonable, taking into account the only partially quenched orbital moment for a HS-d^7 system. The low-temperature slope of the μ_{eff} versus temperature curve indicates weak antiferromagnetic coupling, which is overcome at

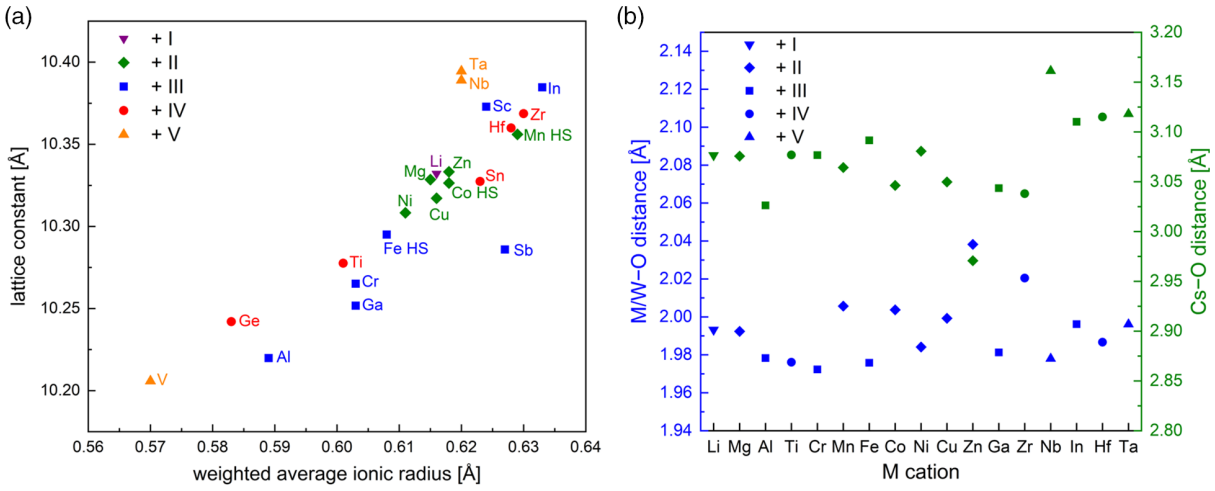

Figure 3. a) Correlation of lattice constants of $CsM_xW_{2-x}O_6$ compounds and weighted average ionic radii of M/W cations. b) Selected interatomic distances. All ionic radii are for sixfold coordination and are taken from Shannon.[50]

© 2021 The Authors. Energy Technology published by Wiley-VCH GmbH

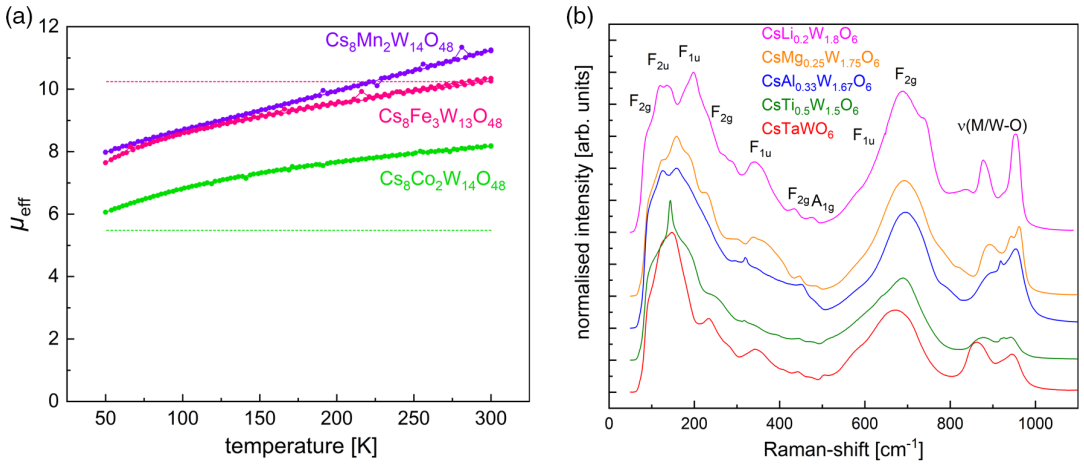

Figure 4. a) Temperature dependence of the effective magnetic moment μ_{eff} of selected $CsM_xW_{2-x}O_6$ compounds (horizontal lines denote spin-only estimates for 2× HS Co(II) and 3× HS Fe(III)). b) Raman spectra of selected samples; assignment of Raman bands was performed according to Mączka et al.[51]

high temperature. In contrast, the effective magnetic moment for $CsMn_{0.25}W_{1.75}O_6$ ($Cs_8Mn_2W_{14}O_{48}$ considering the entire unit cell) is significantly larger than expected for two uncoupled HS-d^5 ions. Moreover, the curve shows no signs of a constant magnetic moment as it would be expected for uncoupled magnetic centers (Curie behavior) in the investigated temperature range. This may indicate the presence of a very small amount of a ferromagnetic impurity.

Structural changes also become apparent in the Raman spectra below 200 cm^{-1} (Figure 4b and Figure S13, Supporting Information): these bands can be assigned to translational modes, narrow bands belong to translational modes of Cs, whereas the statistical occupation of the 16*c* sites results in broad Raman bands belonging to translational modes of M and W.[51] Although these modes are normally Raman inactive, their presence has been explained by breaking of the local symmetry due to substitutional disorder in the 16*c* sites, resulting in the *R*3*m* space group.[51] Moreover, displacement of Cs along ⟨111⟩ direction has been reported for $CsTi_{0.5}W_{1.5}O_6$, along with a locally correlated displacement of Cs along ⟨110⟩ direction.[52] These local disturbances of the ideal defect-pyrochlore crystal structure seem to be dependent on the size and charge of the M cation, thus resulting in different translational modes and Raman bands. Raman bands belonging to bending MO_6/WO_6 modes between 250 and 500 cm^{-1} are mostly similar between different $CsM_xW_{2-x}O_6$ compounds. Two strong Raman bands belonging to MO_6/WO_6 stretching modes can be observed between 650 and 800 cm^{-1}.[51] In addition, two or three Raman bands are discernible between 800 and 1000 cm^{-1}; these bands can be assigned to stretching modes of shorter-than-normal M—O and W—O bonds, resulting from a rearrangement of the oxygen sublattice, which in turns results from vacancies at the M/W 16*c* site.[51,53] In general, lowering the oxidation state of M seems to result in an intensity increase of these bands, alluding to a higher amount of defects for these materials. It is noteworthy that for some M cations (such as Mn^{2+}, Co^{2+}, and Ni^{2+}, Figure S13, Supporting Information) these bands increase significantly in intensity, suggesting a higher amount of defects within these compounds.

The changing M/W ratios were confirmed with energy-dispersive X-ray (EDX) spectroscopy (**Figure 5**a): measured and theoretically expected values are in quite good accordance; EDX measurements are hindered by the low amounts of M—especially for M^{2+} and M^{3+} with 2.8 and 3.7 at%, respectively. Moreover, Li cannot be detected with EDX. Since the measured values scatter statistically above and below the theoretical values, no systematic aberration is discernible. The largest discrepancy is visible for Ta, but this can be explained with the poor energy resolution of EDX: Ta and W are adjacent elements in the periodic system and their X-ray energies are highly similar to each other, thus resulting in a large error.[54] Another discrepancy is visible for Al, the reason could be the overlap of the Al Kα line with a minor W X-ray line.[54]

2.2. Morphological, Optical, and Electronic Characterization

Because the photocatalytic activity directly depends on the surface area, physisorption measurements were used to determine the Brunauer-Emmett-Teller (BET) surface areas of our samples. Because of small surface areas due to the high temperatures used in the syntheses, krypton was used as the adsorbate. Most surface areas are between 0.5 and 2 $m^2\,g^{-1}$ (Figure 5b); however, some samples (with M = Nb^{5+}, Hf^{4+}, Ta^{5+}) have higher surface areas of up to 4.9 $m^2\,g^{-1}$.

The morphology of all samples is not fully homogeneous: well-formed octahedrally shaped particles with smooth surfaces are mixed with smaller, irregularly formed particles (**Figure 6** and Figure S14, S15, S16 and S17 Supporting Information). The overall morphology includes large macropores, whose formation can be attributed to the formation of gases during the combustion reaction.[55]

The optical properties of $CsM_xW_{2-x}O_6$ are found to be crucially dependent on the electron configuration of the M cation: $CsM_xW_{2-x}O_6$ compounds in which M cations have either a d^0 or a d^{10} electron configuration have identical bandgaps of 3.5 eV—within the experimental uncertainty (**Figure 7**a and Figure S18, Supporting Information). The reason for this is that the

© 2021 The Authors. Energy Technology published by Wiley-VCH GmbH

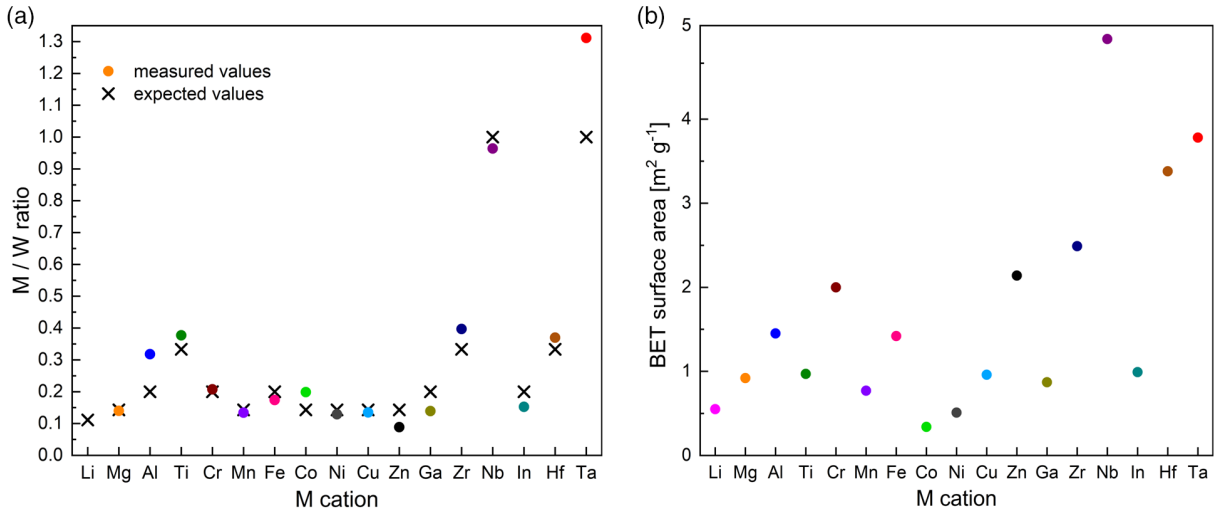

Figure 5. a) Ratios of M/W as measured by EDX; colored circles indicate measured values, whereas black crosses indicate expected values. b) BET surface areas determined by Kr physisorption.

transition from the valence band (VB) to the CB is from O 2*p* states to W 5*d* states without direct involvement of M states.[16,18]

Flat band potentials were estimated using Mott–Schottky plots (Figure 7b and Figure S18, Supporting Information). The flat band potentials of these samples are highly similar, with a mean value of −0.8 V (vs RHE) and a standard deviation of ±0.2 V, further suggesting that the VB-to-CB transition is unaffected by M states. Similar flat band potentials have been reported before for $CsNbWO_6$ and $CsTaWO_6$.[18] The observed deviation could very well be a consequence of measurement errors because Mott—Schottky analysis is, strictly speaking, only valid for smooth surfaces. Moreover, the slopes of all samples are nearly identical, suggesting also an identical charge carrier density—assuming that the relative permittivities and the electrochemically active surface areas are also identical.

Opposed to these results are $CsM_xW_{2-x}O_6$ compounds in which M has partially occupied *d* states (hereafter labeled as d^n): these compounds not only have smaller bandgaps ranging from 2.0 to 2.9 eV (**Figure 8**a), but most also exhibit discrete but broad bands in the visible and near-IR (NIR) region (Figure 8b), which can be attributed to *d*–*d* transitions.[56] The exception is $CsMn_{0.25}W_{1.75}O_6$, which shows only a bandgap transition and no *d*–*d* transitions, because the latter would be spin forbidden. These samples are colored with the actual color being a combination of the bandgap transition and the *d*–*d* bands (if present): $CsCr_{0.33}W_{1.67}O_6$ is light brown, $CsMn_{0.25}W_{1.75}O_6$ is dark red, $CsFe_{0.33}W_{1.67}O_6$ is grayish-green, $CsCo_{0.25}W_{1.75}O_6$ is dark green, $CsNi_{0.25}W_{1.75}O_6$ is yellow, and $CsCu_{0.25}W_{1.75}O_6$ is green-grayish (Figure S19, Supporting Information). The diminished bandgaps of these samples can be explained by either a raised VB, a lowered CB, or a combination of both, as examples in the literature have shown: Dey et al. have analyzed the optical properties of MWO_4 wolframites (M = Mg^{2+}, Mn^{2+}, Co^{2+}, Ni^{2+}, Cu^{2+}, and Zn^{2+}).[56] $MgWO_4$ and $ZnWO_4$ have reported bandgaps of ≈4 eV as opposed to the bandgaps of the other four compounds—with d^n electron configuration—which are reported to be between 2.3 and 3.0 eV. These lower bandgaps are explained by partially occupied M 3*d* states that are located above the O 2*p* states, resulting in a transition from M 3*d* to W 5*d*. Their reasoning is supported by band calculations for $MnWO_4$ that show the Mn^{2+} 3*d* states to be located above the O 2*p* states. In addition, the energy difference between O 2*p* and W 5*d* in $MnWO_4$ is calculated to be ≈3.7 eV, which is similar to the calculated bandgap of $MgWO_4$ of 3.6 eV and the experimentally determined bandgaps for $MgWO_4$ and $ZnWO_4$ of ≈4.0 eV. Calculations for $FeWO_4$ and $CoWO_4$ have shown that the CB minima consist of empty Fe 3*d* and Co 3*d* states, respectively, whereas occupied Fe 3*d* and Co 3*d* states are contributing to the upper VB.[57] However, optical and photoelectron measurements for $MnWO_4$, $FeWO_4$, and $NiWO_4$ single crystals suggest that M 3*d* and O 2*p* are hybridized in the VB, whereas the CB minimum consist of Ni 3*d* for $NiWO_4$, but of Fe 4*s* and Mn 4*s* for $FeWO_4$ and $MnWO_4$, respectively.[58]

Mott–Schottky analyses for $CsM_xW_{2-x}O_6$ (M = Cr^{3+}, Fe^{3+}, Ni^{2+} and Cu^{2+}) have resulted in flat band potentials of −0.7 and −0.8 V (vs RHE) (Figure S20, Supporting Information). Conservation of the flat band potential across the entire series of $CsM_xW_{2-x}O_6$ compounds strongly suggests that the diminished bandgaps are a consequence of a raised VB instead of a lowered CB. However, the Mott–Schottky plots for $CsMn_{0.25}W_{1.75}O_6$ and $CsCo_{0.25}W_{1.75}O_6$ show only a small linear region, making a reliable flat band estimation problematic.

2.3. Photocatalytic Hydrogen Production

The photocatalytic activity of $CsM_xW_{2-x}O_6$ with a bandgap of 3.5 eV was tested by sacrificial hydrogen evolution in water/methanol under UV light illumination; due to their comparatively larger bandgaps $CsNi_{0.25}W_{1.75}O_6$ and $CsCu_{0.25}W_{1.75}O_6$ were also included (**Figure 9** and S21, Supporting Information). All samples show sustained hydrogen evolution upon illumination even without a cocatalyst (time interval 0–2 h). After in-situ photodeposition of Rh as the cocatalyst, the photocatalytic activity increased significantly (2–4 h). The additional photodeposition of Cr_2O_3 results in decreased activities (4–6 h), which is expected because photogenerated electrons

© 2021 The Authors. Energy Technology published by Wiley-VCH GmbH

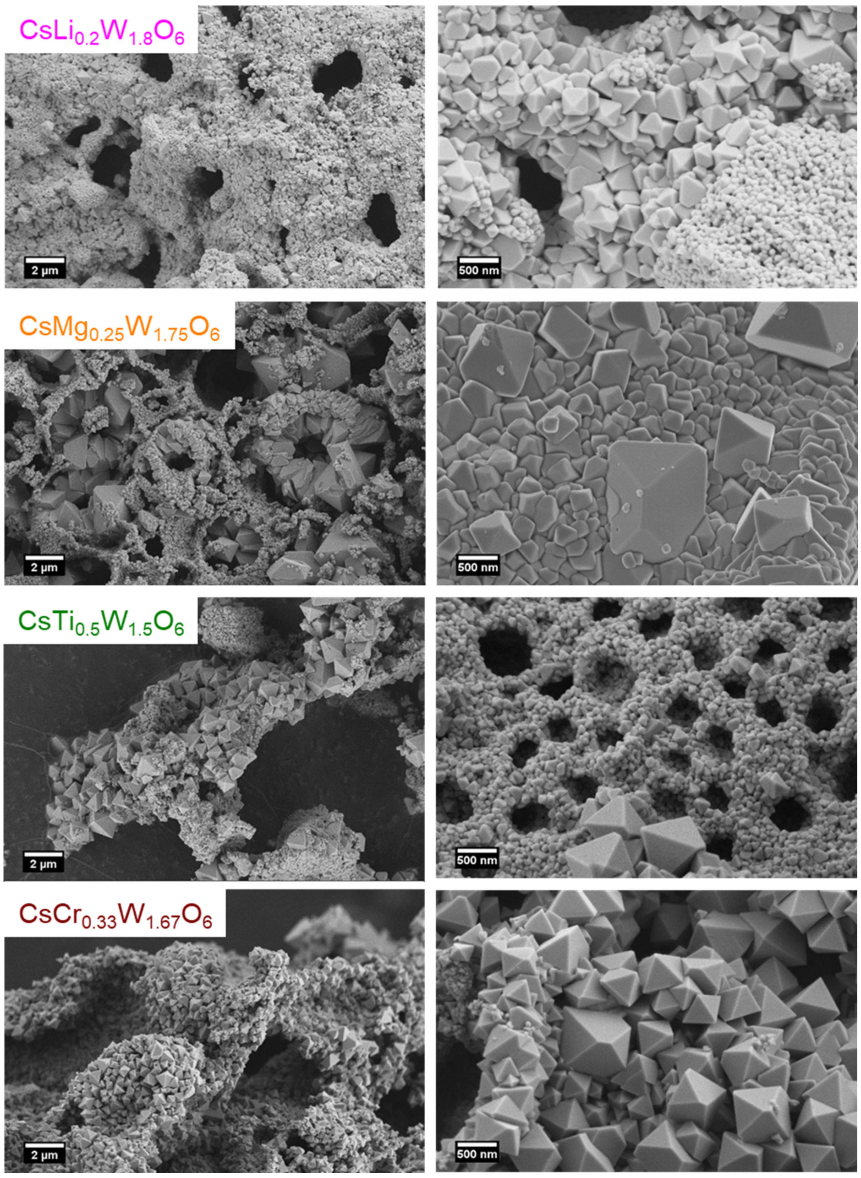

Figure 6. SEM images of $CsLi_{0.2}W_{1.8}O_6$ (first row), $CsAl_{0.33}W_{1.67}O_6$ (second row), $CsTi_{0.5}W_{1.5}O_6$ (third row), and $CsCr_{0.33}W_{1.67}O_6$ (fourth row).

are consumed for chromium reduction.[59] After the illumination is stopped, hydrogen evolution decreases to zero (6–7 h). Some samples—for example, $CsTi_{0.5}W_{1.5}O_6$—show decreasing hydrogen evolution after photodeposition of Rh, the likely reason is the photo-oxidation of the cocatalyst; the same phenomenon has also been observed for Pt nanoparticles.[60] The different activities of the samples cannot be explained purely by their different surface areas; for example, the BET areas of $CsMg_{0.25}W_{1.75}O_6$ and $CsTi_{0.5}W_{1.5}O_6$ are nearly identical (Figure 5b). Additionally, their bandgaps and flat band potentials are also identical within the experimental uncertainty (Figure 7). However, the difference in photocatalytic activity could be explained by the different defect concentrations inferred from the Raman spectra: the samples with the highest activities also show the smallest Raman bands in the range from 800 to 1000 cm^{-1}, which ultimately result from vacancies at the M/W site. We conclude, therefore, that for this class of materials the amount of defects seems to be the reason for the differing activities in sacrificial hydrogen evolution.

To ascertain the photochemical stability of these materials, all samples were recovered after photocatalysis and analyzed: neither the XRD patterns nor the Raman spectra of those samples irradiated with UV light show any changes as compared to before photocatalysis (Figure S22 and S23, Supporting Information). The optical bandgaps have also not changed; the slight gray tint can be explained by the photodeposition of the cocatalyst (Figure S24, Supporting Information).

Some selected samples were also used in overall water splitting experiments, that is, in pure water without any sacrificial agent; however, all were found to be inactive (not shown). To date, the only reported water splitting with defect-pyrochlores in the literature is from Ikeda et al., who used a high-power, ultrahigh-pressure Hg lamp under reduced pressure to achieve

© 2021 The Authors. Energy Technology published by Wiley-VCH GmbH

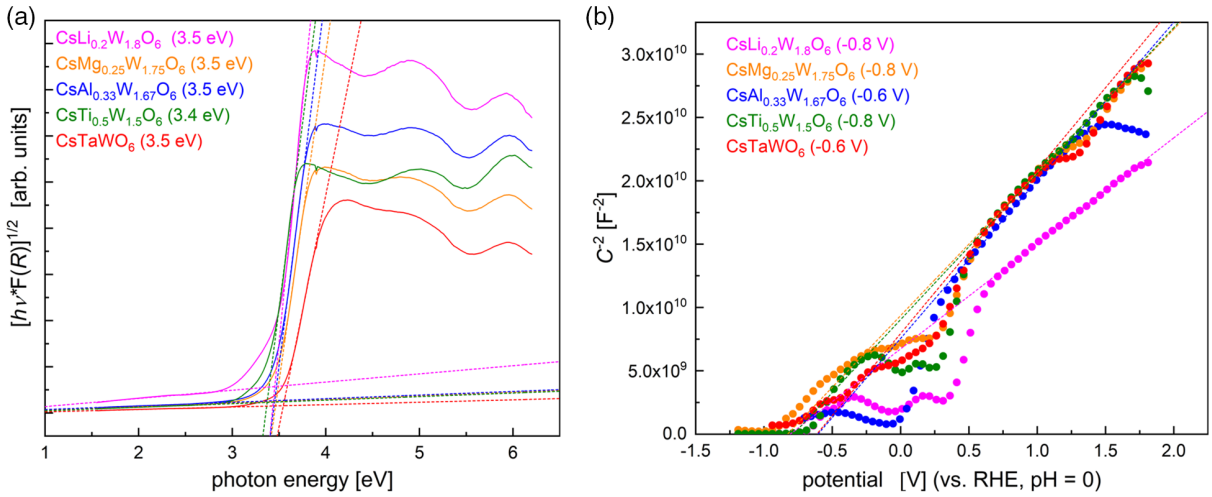

Figure 7. a) Tauc plots for indirect bandgaps and b) Mott–Schottky plots for selected $CsM_xW_{2-x}O_6$ compounds. Bandgaps and flat band potentials are directly written in the respective graphs.

overall water splitting for $AMWO_6$ (A = Rb, Cs and M = Nb, Ta).[16] The likely reason for the inactivity of these materials is the prevalence of defects as shown by Raman spectroscopy, which could act as efficient recombination centers.

Also interesting are the low photocatalytic activities of $CsNi_{0.25}W_{1.75}O_6$ and $CsCu_{0.25}W_{1.75}O_6$ even though these samples have smaller bandgaps and should therefore be able to absorb more photons compared to the other samples. The diminished activity observed instead indicates inhibiting effects counteracting the increased photon absorption. Moreover, all six samples with partially occupied M 3*d* states (M = Cr^{3+}, Mn^{2+}, Fe^{3+}, Co^{2+}, Ni^{2+}, and Cu^{2+}) have also been used in sacrificial hydrogen evolution in simulated solar light; however, no hydrogen could be detected (not shown). This seems peculiar because $KFe_{0.33}W_{1.67}O_6$ has been reported to be active in sacrificial hydrogen evolution in direct solar light.[43] It is important to note that no signs of decomposition could be observed for samples with partially filled M 3*d* states: XRD patterns and Raman spectra do not show changes (Figure S25, Supporting Information) and UV/vis/NIR spectra also show no changes in bandgaps or absorption bands (Figure S26, Supporting Information).

Our results would indicate that M atoms with partially filled M 3*d* states actually inhibit photocatalytic activity. Open-shell dopants have been previously discussed as both promoter and inhibitor of photocatalytic activity.[61,62]

A VB-to-CB excitation involving these partially occupied 3*d* states could likely result in shorter charge carrier lifetimes: for example, the decay half-time of TiO_2 has been reported to be 6.2 ns as compared to the 3 ps in α-Fe_2O_3.[63] A higher recombination rate is corroborated by the Raman spectra of these samples: The defect amount at the M/W sites is larger in the colored samples than for the uncolored samples (Figure 4b and Figure S12, Supporting Information). An additional problem is the potential existence of trap states: Cu^{2+} incorporation in the defect-pyrochlore

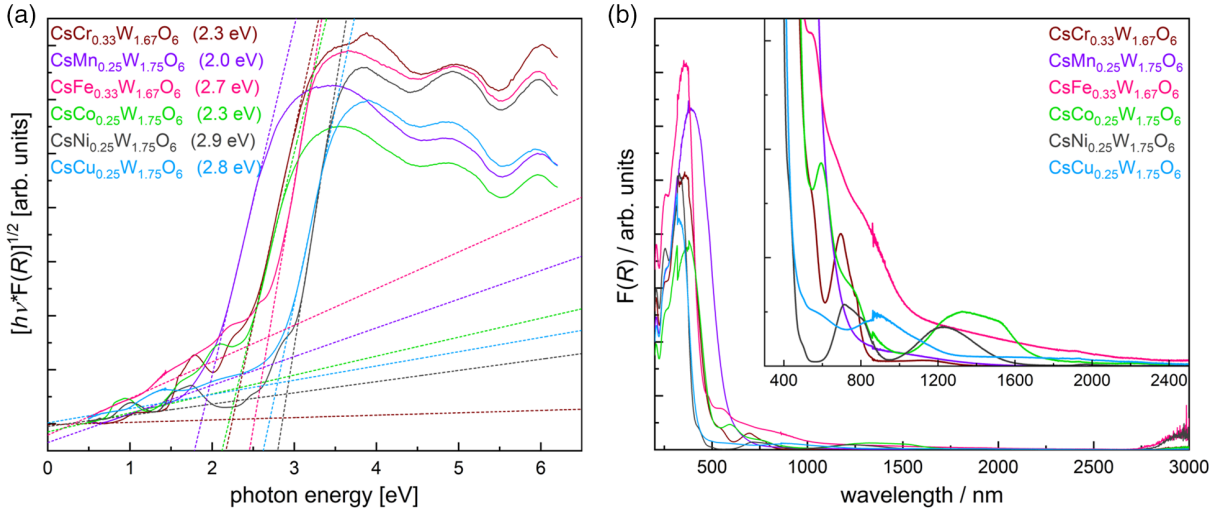

Figure 8. a) Tauc plots and b) Kubelka–Munk absorption spectra of $CsM_xW_{2-x}O_6$ compounds with partially occupied *d* levels. The inset shows a magnification of the absorption at higher wavelengths.

© 2021 The Authors. Energy Technology published by Wiley-VCH GmbH

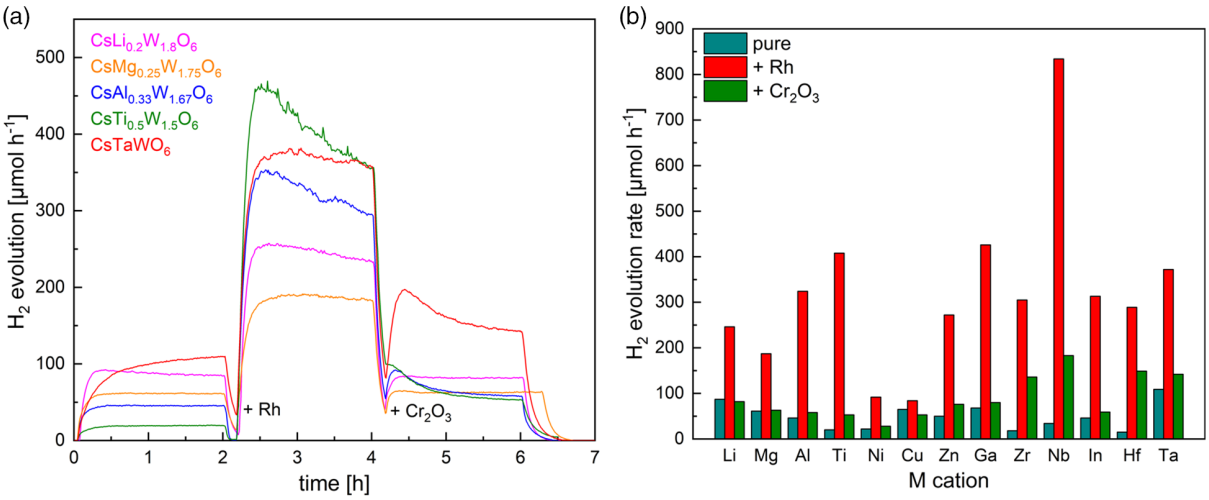

Figure 9. a) Sacrificial hydrogen evolution of selected samples and b) and overview of all samples.

$KNbTeO_6$ has been reported to result in trap states in the middle of the bandgap that act as recombination centers.[21] All these drawbacks relate to the availability of multiple (stable) oxidation states of these M ions—especially for Cr and Mn: these could also act as (additional) trap states, for electrons as well as for holes.[62,64] A reliable identification of oxidation states of these ions using XPS however is highly problematic due to complex multiplet splitting.[65]

3. Conclusion

We have successfully used a sol–gel synthesis followed by combustion and annealing in air to comprehensively investigate the elemental diversity of tungsten-based defect-pyrochlores $CsM_xW_{2-x}O_6$. Overall, 17 phase-pure compounds—8 of them unknown so far—and a further 5 compounds with impurities could be synthesized, thus unveiling the high elemental multifariousness of the defect-pyrochlore crystal structure. The lattice constant of the cubic crystal structure depends nearly linearly on the ionic radius of the M cation. Furthermore, the optical and electronic properties are highly dependent on the electron configuration of M: If M has d^0 or d^{10} electron configuration, bandgaps and flat band potentials are nearly identical with 3.5 eV and −0.8 V (vs RHE), respectively. However, if M has partially occupied M 3*d* states the compounds become colorful and the bandgaps are between 2.0 and 2.9 eV due to a change of the VB-to-CB transition. Although d^0 or d^{10} compounds are photocatalytically active in UV light, the photocatalytic activity seems to be dependent mainly on defect concentrations. In contrast, samples with partially occupied M 3*d* states which have been found to be photocatalytically inactive in simulated solar light; the reason seems to be a higher prevalence of defects.

4. Experimental Section

Synthesis: All used chemicals are listed in Table S1, Supporting Information. The exact amounts of every substance and for every synthesis can be seen in Table S2 and S3, Supporting Information.

Three equivalents (equiv.) of citric acid hydrate and two equiv. EDTA were added to water (120 mL); ammonium hydroxide solution was then added until both solids were dissolved. The solution was then acidified with concentrated nitric acid to a pH of 4–5. Then hydrogen peroxide (30%, 10 mL) was added; however, hydrogen peroxide was omitted if the M cation was Co^{2+} or Mn^{2+}. In the next step, $CsNO_3$ was added and the solution heated to 95 °C. During heating, the M precursor was added (see also Table S2 and S3, Supporting Information). After dissolution of the M precursor, ammonium tungsten oxide was added: ammonium *para* tungsten oxide was used for syntheses, in which M was M^{5+}, M^{4+}, or M^{3+}, whereas ammonium *meta* tungsten oxide was used for M^{2+} and M^{1+} due to the higher solubility. The solution was heated until the volume decreased to ≈20 mL and then transferred into a porcelain bowl, placed in a heating mantle, and heated to 350 °C while stirring manually. The black solid remaining after combustion was ground into a powder and annealed at temperatures from 500–900 °C in air to investigate the formation temperatures and the general thermal stability of these compounds. The samples used for further characterization and photocatalytic experiments were all annealed at 800 °C with the following exceptions: $CsLi_{0.2}W_{1.8}O_6$ was annealed at 900 °C because the higher temperature is necessary for a phase-pure compound, whereas $CsZr_{0.5}W_{1.5}O_6$ and $CsHf_{0.5}W_{1.5}O_6$ were annealed at only 600 °C to avoid thermal decomposition. The annealing time was always 10 h and the heating rate was fixed to 5 °C min^{-1}.

Characterization: XRD was measured with either an Empyrean or an X'Pert Pro (both Malvern PANalytical) diffractometer using Cu Kα radiation. Theoretical diffraction patterns were calculated based on the information published by Knyazev et al.[24] This information was also used for Rietveld refinements using the program FullProf.[66,67] Peak shapes were modeled with a Thompson–Cox–Hastings pseudo-Voigt function with asymmetry correction;[68] the background was estimated using a Chebyshev polynomial. Instrumental broadening was determined with a LaB_6 standard (NIST SRM 660c). Refined parameters are: scale, zero shift, lattice constants, FWHM parameters (including asymmetry correction and anisotropic size broadening), isotropic thermal displacement parameters, and atom positions (only for O because cations are fixed on special positions); all other parameters were fixed.

XPS was measured with a VersaProbe III Scanning XPS Microprobe (Physical Electronics PHI) with a monochromatized Al Kα source. High-resolution spectra were measured with a step size of 0.1 eV, a pass energy of 26 eV, and a step time of 50 ms; the beam diameter was 100 µm. Data were analyzed with CasaXPS; Gaussian–Lorentzian (GL30) line shapes and Shirley backgrounds were used. The C 1*s* signal was set to 284.8 eV for charge correction.

Magnetic measurements were performed with a MPMS-XL SQUID (Quantum Design) at a constant field strength of 5000 Oe. Samples were

© 2021 The Authors. Energy Technology published by Wiley-VCH GmbH

placed in a gelatine capsule held by a plastic straw; raw data were corrected for the diamagnetism of the sample holder.

Diffuse-reflection UV/vis/NIR spectra were recorded with a Lambda 750 (Perkin-Elmer) spectrometer and a praying mantis mirror unit (Harrick). A spectralon pellet was used as the white standard. Diffuse reflectance was converted into absorbance using the Kubelka–Munk function; bandgaps were estimated with Tauc plots.[69]

Raman spectra were measured with a LabRam system version 010 (Horiba Jobin Yvon), equipped with a 633 nm laser with a power of 11.5 mW.

Physisorption measurements were performed with an ASIQ-MP-MP-AG instrument (Anton Paar QuantaTec) using krypton at 77 K. Surface areas were determined by the BET method.

Scanning electron microscopy (SEM) images were recorded with a Leo 1530 (Zeiss). Samples were sputter-coated with platinum using a 208HR sputter coater (Cressington) prior to measurements. EDX was measured on the SEM described previously using an Ultradry-EDX detector (Thermo Fisher Scientific). Several different spots were measured and averaged for every sample.

Mott–Schottky measurements were recorded with a Zennium potentiostat (Zahner Elektrik) at a frequency of 1000 Hz in 0.1 mol L^{-1} Na_2SO_4 solution (pH 5.2). The valid frequency range was determined with electrochemical impedance measurements in a range from 100 kHz to 1 Hz. A glass junction filled with 3 mol L^{-1} NaCl solution was used to protect the Ag/AgCl reference electrode. Working electrodes were prepared by spray coating a dispersion (100 mg sample in 30 mL ethanol) on fluorine-doped tin oxide (FTO)-coated glass slides (20 mm × 30 mm, XOP Glass) heated to 250 °C. The dispersion was ultrasonicated prior to spray coating. The prepared electrodes were contacted with conductive copper tape and mounted into a PECC-2 cell (Zahner Elektrik).

Photocatalytic Experiments: For photocatalytic experiments using UV light, 300 mg sample were dispersed in water (550 mL) and methanol (50 mL) using ultrasonication and filled into a homemade double-walled inner-immersion-type reactor. A double-walled quartz glass inlet was used to house a 700 W TQ718 mercury lamp (Peschl Ultraviolet); lamp power during measurements was adjusted to 350 W. A constant temperature within the reactor of 10 °C was maintained with a Proline RP845 (Lauda) thermostat. The reactor was flushed with an argon 5.0 flow of 100 standard cubic centimeters per minute (sccm) using an El-Flow Select mass flow controller (Bronkhorst). Evolved gases were detected with a HPR-20 Q/C (Hiden Analytics) quadrupole mass spectrometer (MS). After 2 h, the lamp was switched off and Na_3RhCl_6 (Aldrich) solution was injected through a rubber sealing without opening the reactor—resulting in a cocatalyst loading of 3 µmol Rh per mmol sample. After waiting for 10 min to ensure a homogeneous distribution within the reactor, the lamp was restarted for in situ photodeposition. After 4 h, 3 µmol Cr_2O_3 per mmol sample was photodeposited using K_2CrO_4 (Alfa Aesar). After 6 h the lamp was switched off and after 7 h the measurement was stopped. Water-splitting experiments were performed with the same setup: however, the sample was dispersed in 600 mL pure water.

For some samples, photocatalytic measurements were also performed in simulated solar light using an Oriel Sol1A solar simulator (Newport) with an AM 1.5G filter. The samples (200 mg) were dispersed in water (135 m) and methanol (15 mL) using ultrasonication and filled into a homemade glass reactor with a quartz glass window on top. A constant temperature of 20 °C was maintained with an ECO RE 1050G (Lauda) thermostat. The reactor was flushed with an argon 5.0 flow of 100 sccm, which was reduced to 25 sccm during the measurement. A GC2014 (Shimadzu) equipped with a thermal conductivity detector and a ShinCarbon ST column (Restek) was used to detect the evolved gases. Argon 5.0 was used as the carrier and detector gas. At the start of the measurement, 3 µmol Rh per mmol sample was photodeposited in situ.

Supporting Information

Supporting Information is available from the Wiley Online Library or from the author.

Acknowledgements

The authors would like to thank Dr. Jana Timm for physisorption measurements and Anja Hofmann for SEM images and EDX measurements (both University of Bayreuth). The authors also thank the Bavarian Polymer Institute (BPI) Keylab "Electron and Optical Microscopy" for use of the SEM and the Keylab "Device Engineering" for use of the XPS. M.W. and R.M. gratefully acknowledge funding in the Emmy-Noether program of the German Research Foundation DFG (MA 5392/3-1).

Open access funding enabled and organized by Projekt DEAL.

Conflict of Interest

The authors declare no conflict of interest.

Data Availability Statement

Research data are not shared.

Keywords

defect pyrochlores, photocatalysis, visible light absorption

Received: April 15, 2021
Revised: July 23, 2021
Published online: September 1, 2021

[1] D. Babel, G. Pausewang, W. Viebahn, *Z. Naturforsch., B. J. Chem. Sci.* **1967**, *22*, 1219.
[2] R. M. Biefeld, M. A. Butler, L. J. Azevedo, *Solid State Commun.* **1981**, *38*, 1125.
[3] M. A. Subramanian, R. Subramanian, A. Clearfield, *Solid State Ionics* **1985**, *15*, 15.
[4] R. Hinrichs, G. Tomandl, J. A. H. da Jornada, *Solid State Ionics* **1995**, *77*, 257.
[5] N. Binesh, V. Bhat, S. V. Bhat, *Solid State Ionics* **1996**, *86–88*, 665.
[6] T. Siritanon, G. Laurita, R. T. Macaluso, J. N. Millican, A. W. Sleight, M. A. Subramanian, *Chem. Mater.* **2009**, *21*, 5572.
[7] J. Li, T. Siritanon, J. K. Stalick, A. W. Sleight, M. A. Subramanian, *Inorg. Chem.* **2011**, *50*, 5747.
[8] A. Waehayee, N. Chanlek, P. Kidkhunthod, H. Nakajima, S. Suthirakun, T. Siritanon, *Phys. Rev. B* **2019**, *100*, 045132.
[9] M. Ohtaki, S. Miyaishi, *J. Electron. Mater.* **2013**, *42*, 1299.
[10] K. Mizuta, M. Ohtaki, *J. Electron. Mater.* **2016**, *45*, 1695.
[11] S. V. Streltsov, I. I. Mazin, R. Heid, K. P. Bohnen, *Phys. Rev. B* **2016**, *94*, 241101.
[12] Y. N. Han, S. Jiao, M. Xu, Y. Xu, G. Pang, S. Feng, *RSC Adv.* **2014**, *4*, 24142.
[13] D. Zhao, J. Zhao, Y. C. Fan, Z. Ma, R. J. Zhang, B. Z. Liu, *Phys. B* **2018**, *539*, 97.
[14] S.-H. Choe, C.-J. Yu, M. Choe, Y.-H. Kye, Y.-N. Han, G. Pang, *Phys. Rev. B* **2020**, *102*, 035131.
[15] Y. N. Han, S. Jiao, M. Xu, G. Pang, S. Feng, *RSC Adv.* **2014**, *4*, 14357.
[16] S. Ikeda, T. Itani, K. Nango, M. Matsumura, *Catal. Lett.* **2004**, *98*, 229.
[17] L. Schwertmann, M. Wark, R. Marschall, *RSC Adv.* **2013**, *3*, 18908.
[18] L. Schwertmann, A. Grünert, A. Pougin, C. Sun, M. Wark, R. Marschall, *Adv. Funct. Mater.* **2015**, *25*, 905.
[19] X. Zeng, Y. Chen, S. Jiao, Z. Fang, B. Wang, G. Pang, S. Feng, *New J. Chem.* **2018**, *42*, 5753.

© 2021 The Authors. Energy Technology published by Wiley-VCH GmbH

[20] T. Weller, L. Deilmann, J. Timm, T. S. Dörr, P. A. Beaucage, A. S. Cherevan, U. B. Wiesner, D. Eder, R. Marschall, *Nanoscale* **2018**, *10*, 3225.
[21] A. Waehayee, P. Watthaisong, S. Wannapaiboon, N. Chanlek, H. Nakajima, J. Wittayakun, S. Suthirakun, T. Siritanon, *Catal. Sci. Technol.* **2020**, *10*, 978.
[22] A. Castro, I. Rasines, X. M. Turrillas, *J. Solid State Chem.* **1989**, *80*, 227.
[23] S. F. Mayer, H. Falcón, M. T. Fernández-Díaz, J. A. Alonso, *Crystals* **2018**, *8*, 368.
[24] A. V. Knyazev, N. G. Chernorukov, N. N. Smirnova, N. Y. Kuznetsova, A. V. Markin, *Thermochim. Acta* **2008**, *470*, 47.
[25] P. W. Barnes, P. M. Woodward, Y. Lee, T. Vogt, J. A. Hriljac, *J. Am. Chem. Soc.* **2003**, *125*, 4572.
[26] A. V. Knyazev, M. Maczka, N. Y. Kuznetsova, *Thermochim. Acta* **2010**, *506*, 20.
[27] D. W. Murphy, R. J. Cava, K. Rhyne, R. S. Roth, A. Santoro, S. M. Zahurak, J. L. Dye, *Solid State Ionics* **1986**, *18–19*, 799.
[28] G. Rodríguez-Gattorno, L. F. del Castillo, E. Torres-García, *Thermochim. Acta* **2005**, *435*, 176.
[29] M. Weiss, R. Marschall, *Nanoscale* **2018**, *10*, 9691.
[30] M. L. Veiga, A. Jerez, M. Gaitán, C. Pico, *Thermochim. Acta* **1988**, *124*, 25.
[31] S. Garía-Martin, M. L. Veiga, A. Jerez, M. Gaitán, C. Pico, *J. Chem. Soc., Dalt. Trans.* **1988**, 2141.
[32] T. Kar, R. N. P. Choudhary, *J. Phys. Chem. Solids* **2001**, *62*, 1149.
[33] T. Kar, R. N. P. Choudhary, *Mater. Sci. Eng., B* **2002**, *90*, 224.
[34] N. G. Chernorukov, A. V. Knyazev, N. Y. Kuznetsova, S. N. Golubev, *Russ. J. Inorg. Chem.* **2008**, *53*, 1303.
[35] N. G. Chernorukov, A. V. Knyazev, N. Y. Kuznetsova, I. V. Ladenkov, *Phys. Solid State* **2011**, *53*, 292.
[36] D. G. Fukina, E. V. Suleimanov, R. P. Yavetskiy, G. K. Fukin, A. V. Boryakov, E. N. Borisov, E. V. Borisov, S. I. Surodin, N. V. Saharov, *J. Solid State Chem.* **2016**, *241*, 64.
[37] M. Hervieu, B. Raveau, *C. R. Seances Acad. Sci., Ser. C* **1970**, *271*, 1568.
[38] K. R. Whittle, G. R. Lumpkin, S. E. Ashbrook, *J. Solid State Chem.* **2006**, *179*, 512.
[39] G. Le Flem, R. Salmon, *C. R. Seances Acad. Sci., Ser. C* **1970**, *271*, 1182.
[40] G. J. Thorogood, B. J. Kennedy, V. K. Peterson, M. M. Elcombe, G. J. Kearley, J. V. Hanna, V. Luca, *J. Solid State Chem.* **2009**, *182*, 457.
[41] R. Guje, G. Ravi, S. Palla, K. N. Rao, M. Vithal, *Mater. Sci. Eng., B* **2015**, *198*, 1.
[42] M. Weiss, B. Wirth, R. Marschall, *Inorg. Chem.* **2020**, *59*, 8387.
[43] G. Ravi, S. Palla, N. K. Veldurthi, J. R. Reddy, A. Hari Padmasri, M. Vithal, *Int. J. Hydrogen Energy* **2014**, *39*, 15352.
[44] G. Ravi, P. Shrujana, S. Palla, J. R. Reddy, R. Guje, R. Velchuri, M. Vithal, *Micro Nano Lett.* **2014**, *9*, 11.
[45] R. J. Cava, R. S. Roth, T. Siegrist, B. Hessen, J. J. Krajewski, W. F. Peck, *J. Solid State Chem.* **1993**, *103*, 359.
[46] D. Hirai, M. Bremholm, J. M. Allred, J. Krizan, L. M. Schoop, Q. Huang, J. Tao, R. J. Cava, *Phys. Rev. Lett.* **2013**, *110*, 166402.
[47] Y. Okamoto, H. Amano, N. Katayama, H. Sawa, K. Niki, R. Mitoka, H. Harima, T. Hasegawa, N. Ogita, Y. Tanaka, M. Takigawa, Y. Yokoyama, K. Takehana, Y. Imanaka, Y. Nakamura, H. Kishida, K. Takenaka, *Nat. Commun.* **2020**, *11*, 3144.
[48] F. Garbassi, *Surf. Interface Anal.* **1980**, *2*, 165.
[49] B. O. Loopstra, H. M. Rietveld, *Acta Crystallogr. Sect. B Struct. Crystallogr. Cryst. Chem.* **1969**, *25*, 1420.
[50] R. D. Shannon, *Acta Crystallogr., Sect. A: Cryst. Phys., Diffr., Theor. Gen. Crystallogr.* **1976**, *32*, 751.
[51] M. Mączka, A. V. Knyazev, A. Majchrowski, J. Hanuza, S. Kojima, *J. Phys.: Condens. Matter* **2012**, *24*, 195902.
[52] G. J. Thorogood, P. J. Saines, B. J. Kennedy, R. L. Withers, M. M. Elcombe, *Mater. Res. Bull.* **2008**, *43*, 787.
[53] M. L. Sanjuán, C. Guglieri, S. Díaz-Moreno, G. Aquilanti, A. F. Fuentes, L. Olivi, J. Chaboy, *Phys. Rev. B* **2011**, *84*, 104207.
[54] J. A. Bearden, *Rev. Mod. Phys.* **1967**, *39*, 78.
[55] Y. Li, L. Xue, L. Fan, Y. Yan, *J. Alloys Compd.* **2009**, *478*, 493.
[56] S. Dey, R. A. Ricciardo, H. L. Cuthbert, P. M. Woodward, *Inorg. Chem.* **2014**, *53*, 4394.
[57] S. Rajagopal, V. L. Bekenev, D. Nataraj, D. Mangalaraj, O. Y. Khyzhun, *J. Alloys Compd.* **2010**, *496*, 61.
[58] T. Ejima, T. Banse, H. Takatsuka, Y. Kondo, M. Ishino, N. Kimura, M. Watanabe, I. Matsubara, *J. Lumin.* **2006**, *119–120*, 59.
[59] J. Soldat, R. Marschall, M. Wark, *Chem. Sci.* **2014**, *5*, 3746.
[60] R. Arrigo, M. Hävecker, M. E. Schuster, C. Ranjan, E. Stotz, A. Knop-Gericke, R. Schlögl, *Angew. Chem. Int. Ed.* **2013**, *52*, 11660.
[61] W. Choi, A. Termin, M. R. Hoffmann, *J. Phys. Chem.* **1994**, *98*, 13669.
[62] D. Wang, J. Ye, T. Kako, T. Kimura, *J. Phys. Chem. B* **2006**, *110*, 15824.
[63] S. R. Pendlebury, X. Wang, F. Le Formal, M. Cornuz, A. Kafizas, S. D. Tilley, M. Grätzel, J. R. Durrant, *J. Am. Chem. Soc.* **2014**, *136*, 9854.
[64] F. Ichihara, F. Sieland, H. Pang, D. Philo, A.-T. Duong, K. Chang, T. Kako, D. W. Bahnemann, J. Ye, *J. Phys. Chem. C* **2020**, *124*, 1292.
[65] M. C. Biesinger, B. P. Payne, A. P. Grosvenor, L. W. M. Lau, A. R. Gerson, R. S. C. Smart, *Appl. Surf. Sci.* **2011**, *257*, 2717.
[66] H. M. Rietveld, *J. Appl. Crystallogr.* **1969**, *2*, 65.
[67] J. Rodríguez-Carvajal, *Phys. B Phys. Condens. Matter* **1993**, *192*, 55.
[68] P. Thompson, D. E. Cox, J. B. Hastings, *J. Appl. Crystallogr.* **1987**, *20*, 79.
[69] J. Tauc, R. Grigorovici, A. Vancu, *Phys. Status Solidi B* **1966**, *15*, 627.

© 2021 The Authors. Energy Technology published by Wiley-VCH GmbH